Journal of the Serbian Society for Computational Mechanics / Vol. 15 / No. 1, 2021 / pp 1-23
(10.24874/jsscm.2021.15.01.01)

# COMPUTATIONAL MODEL FOR HEART TISSUE WITH DIRECT USE OF EXPERIMENTAL CONSTITUTIVE RELATIONSHIPS

**Miloš Kojić[1,2,3*], M. Milošević[2,4,5], B. Milićević[2,6], V. Geroski[2,6], V. Simić[2,4], D. Trifunović[7], G. Stanković[3,7,8], N. Filipović[2,6]**

[1] Houston Methodist Research Institute, Department of Nanomedicine, Houston, TX 77030
e-mail:mkojic42@gmail.com
[2] Bioengineering Research and Development Center BioIRC Kragujevac, Kragujevac, Serbia
[3] Serbian Academy of Sciences and Arts, 11000 Belgrade, Serbia
[4] Institute for Information Technologies, University of Kragujevac, Kragujevac, Serbia
[5] Belgrade Metropolitan University, Belgrade, Serbia
[6] University of Kragujevac, Faculty of Engineering, Kragujevac, Serbia
[7] Cardiology Department, University Clinical Center of Serbia, Belgrade, Serbia
[8] Faculty of Medicine, University of Belgrade, Belgrade, Serbia
* *corresponding author*

## Abstract

Heart wall tissue plays a crucial role in living organisms by generating the mechanical force for blood flow. This tissue has a complex internal structure comprised mostly of muscle cells, in which biochemical energy is transformed into mechanical active stress under rhythmical electrical excitation. The overall heart functioning depends, among other physiological conditions, on the mechanical properties of the tissue. Over the past centuries, experimental and theoretical investigations have been conducted in order to establish the constitutive laws governing wall tissue behavior. Regarding computational modeling, many material models have been introduced, from simple elastic anisotropic to more sophisticated ones, based on various formulations of strain potentials. We here present a novel computational model that directly employs experimental constitutive relationships. Therefore, we avoid any fitting of material parameters for a selected analytical form of the constitutive law. Hysteretic characteristics of the tissue are included, as well as either incompressibility or compressibility according to experimentally determined curves. Deformation is split into deviatoric and volumetric parts in order to handle compressibility. The correctness and accuracy of the model is demonstrated through simple cases for loading and unloading conditions. Furthermore, the model was implemented for left ventricle (LV) deformation, where the FE mesh was generated from echocardiography recordings. Here, a specific algorithm, which accounts for LV torsion, was introduced to determine trajectories of material points on the internal LV surface. Hysteresis of the constitutive curves was used to calculate mechanical energy of LV wall tissue deformation. For completeness, the fluid flow within the LV was computed as well.

**Keywords:** Mechanics of lung microstructure, multiscale 3D composite finite element, lung tissue material models, surfactant.

## 1. Introduction – a review of constitutive relations for the cardiac tissue

Functioning of the heart depends on a number of different superimposing simultaneous actions, from electrophysiological to pure mechanical, which occur in a fascinating harmony established by the mystery of life itself. Electrical impulses are generated in a group of cells called the sinoatrial node and transferred through the Purkinje fiber network to trigger changes in the cell membrane potential. These changes induce ionic fluxes through membranes, most importantly of calcium, which serves as the main cause of conformational change within the muscle cell sarcomeres to transform the biochemical into mechanical energy. The generated active stress loads the wall tissue producing deformation and heart wall motion. How the wall tissue, as a passive medium, will respond depends on the mechanical characteristic of the wall tissue. This study focuses on the mechanical tissue properties and computational modeling which adequately includes these properties.

Experimental – in vivo and in vitro – and theoretical investigations of the heart tissue characteristics have been continuously intensive over centuries. Experimental findings are usually accompanied by the fitting of parameters to adopted constitutive relationships in analytical form. Here are listed a few typical references and those relevant for the computational procedure introduced in this study. Experimental results from the laboratory of Professor G. A. Holzapfel, University of Graz (Sommer et al., 2015), serve as the basis of this work and will be further described in detail in Section 2. For the completeness of this paper, we present a few typical experiments and the mathematical formulation of the material models for passive heart tissue. A more detailed presentation and discussion of the models is given in (Holzapfel and Ogden, 2009).

In (Yin et al., 1987) a biaxial stretch is performed on material samples of canine myocardium by loading in the fiber and sheet directions (in the sheet plane) with various stretch ratios. The material model parameters were fitted using the following strain-energy functions W:

$$W = C\exp\left(A_x e_{xx}^n + A_x e_{yy}^n\right) \quad \text{or} \quad W = 0.5C\exp\left(A_x e_{xx}^2 + A_x e_{yy}^2 + 2A_4 e_{xx} e_{yy}\right) \tag{1}$$

where $e_{xx}$ and $e_{yy}$ are the Green-Lagrange strains in fiber and sheet directions, respectively; and $C$, $A_x$, $A_y$, and $n$ are the model parameters. Note that the second expression corresponds to the quadratic form of (Fung et al., 1979). In (Guccione et al., 1991) a strain energy function of a form similar to the above was used to study the effects of the fiber direction distribution across the ventricle wall on the stress field within the wall. The numerical investigation was executed using a simple ellipsoidal model of the ventricle, and the computed deformation was matched to the experiments. Regarding the physiological effects of the fiber helicoidal character in the ventricle, it was shown that during the heart cycle the fiber strain, and therefore active stress within fibers, is remarkably uniform over the ventricle wall (Bovendeerd et al., 1992). An insight into the role of geometric distribution of fibers, considered as the kinematics of cardiac mechanics, is presented in a review paper of (Leonard et al., 2012). The above exponential form of W was further often used in applications, sometimes with modifications, e.g. (S. Lin and P. Yin, 1998; Ponnaluri et al., 2017; Klepach et al., 2012; J. Xi et al., 2013). Another form of the strain-energy function, with a determination of material parameters from biaxial experiments, was introduced by (Humphrey et al., 1990). The function is formulated assuming transversely isotropic material with respect to the fiber direction in the undeformed state as the reference configuration,

$$W = C\exp\left(A_x e_{xx}^n + A_x e_{yy}^n\right) \quad \text{or} \quad W = 0.5C\exp\left(A_x e_{xx}^2 + A_x e_{yy}^2 + 2A_4 e_{xx} e_{yy}\right) \tag{2}$$

where $\lambda_f$ is the fiber stretch related to the strain invariant $I_4=\lambda_f^2$; $I_1$=tr**C** is the first invariant of the right deformation tensor **C**=**F**$^T$**F**, **F** is deformation gradient; and $c_1 \ldots c_4$ are material constants fitted from experiments. This form of W is further used with modifications, e.g. in (Ponnaluri et al., 2017; Klepach et al., 2012; J. Xi et al., 2013) it is taken as the exponent in equation (1). An extension of the form (2) to include the contribution of shear stresses is introduced in (Stevens et al., 2003), according to their experimental investigation and following the results of (Dokos et al., 2002; Dokos et al., 2000). We cite here the form of W given in (Stevens et al., 2003) since it will be used within our computational procedure:

$$W=\sum_{i=1}^{3} k_{ii}\frac{e_{ii}^2}{\left(a_{ii}-e_{ii}\right)^{b_{ii}}}+k_{12}\frac{e_{12}^2}{\left(a_{12}-e_{12}\right)^{b_{12}}}+k_{13}\frac{e_{13}^2}{\left(a_{13}-e_{13}\right)^{b_{13}}}+k_{23}\frac{e_{23}^2}{\left(a_{23}-e_{23}\right)^{b_{23}}} \tag{3}$$

where $e_{ij}$ are engineering strains; $k_{ij}$ and $b_{ij}$ are material coefficients determined from uniaxial loading and shear in the three local material directions, which includes the sheet-normal local direction.

A general model based on morphology and structure of tissue, and experiments, is given in (Holzapfel and Ogden, 2009). The strain energy function is formulated as

$$W=\frac{a}{2b}\exp\left[b\left(I_1-3\right)\right]+\sum_{i=f,s}\frac{a_i}{2b_i}\left\{\exp\left[b_i\left(I_{4i}-1\right)^2\right]-1\right\}+\frac{a_{fs}}{2b_{fs}}\left[\exp\left(b_{fs}I_{8fs}^2\right)-1\right] \tag{4}$$

where $a,b,a_i,b_i,a_{fs},b_{fs}$ are material constants, and $I_1$ is the first invariant; $I_{4i}$ and $I_{8fs}$ are strain invariants expressed in the local fiber-sheet coordinate system. The first two terms in (4) correspond to the material stretch, while the last term represents the strain energy due to shear. Note that this general expression, as well as the all above cited, takes into account strain energy due to deformation in the sheet plane of tissue, defined by the fiber unit vector $\mathbf{f_0}$ and sheet unit vector $\mathbf{c_0}$. It is generally accepted that the heart wall can be considered as a thick shell with tangential $\mathbf{f_0}$- $\mathbf{c_0}$ plane and normal $\mathbf{n_0}$, and that the wall mechanical characteristics are governed by the constitutive laws for deformation in the $\mathbf{f_0}$- $\mathbf{c_0}$ plane.

The above general expression for the strain energy was further applied with some modifications. For example, in (Krishnamurthy et al., 2013), the strain energy function is

$$W=\frac{a}{2b}\exp\left[b\left(I_1-3\right)\right]+\frac{a_f}{2b_f}\left\{\exp\left[b_f\left(I_{4f}-1\right)^2\right]-1\right\} \tag{5}$$

The default material parameters of this expression according to (Holzapfel and Ogden, 2009) were scaled to fit the end-diastolic pressure-volume relations in the patient-specific models. In the scaling of parameters, an empirical relation was also used between the unloaded left-ventricular cavity volume and end diastolic pressure, according to (Klotz et al., 2006).

Finally, in this short overview of experimental investigation and formulation of constitutive relations for passive heart tissue, we cite the work of (McEvoy et al., 2018). The authors studied compressibility of the ventricular myocardium by performing experimental research and using constitutive relationships for the macro-continuum and microstructure. The models are based on the general form (3) of the strain-energy function and the stress is split into isotropic and anisotropic parts. For the macro-model, the isotropic stress represents a reduced polynomial of the Yeoh isotropic hyperelastic model, (Yeoh, 1993),

$$\boldsymbol{\sigma}_{iso}=\sum_{i=1}^{3} k_i i\left(J-1\right)^{2i-1}\mathbf{I}+\sum_{i=1}^{3}\mu_i i\left(\bar{I}_1-3\right)^{i-1}\left(\bar{\mathbf{B}}-\frac{1}{3}\bar{I}_1\mathbf{I}\right) \tag{6}$$

where $k_i$ and $\mu_i$ are material parameters; $J$=det**F** is a measure of the volumetric deformation; $\bar{\mathbf{B}} = J^{-2/3}\mathbf{B}$, where **B=FF$^T$** is the left deformation tensor; $\bar{I}_1 = J^{-2/3} I_1$; and **I** is the identity matrix. The anisotropic part of the total stress is expressed according to the general form of the strain-energy (3),

$$\boldsymbol{\sigma}_{aniso} = \sum_{i=f,s} 2a_i \left(I_{4i} - 1\right) \exp\left[b_i \left(I_{4i} - 1\right)^2\right] \mathbf{a}_i \otimes \mathbf{a}_i + a_{fs} I_{8fs} \exp\left(b_{fs} I_{8fs}^2\right) \left(\mathbf{a}_f \otimes \mathbf{a}_s + \mathbf{a}_s \otimes \mathbf{a}_f\right) \tag{7}$$

where $a_i$,$b_i$,$a_{fs}$,$b_{fs}$ are material constants; $\mathbf{a_f}$, $\mathbf{a_s}$ are the fiber and sheet direction unit vectors $\mathbf{f}_0$ and $\mathbf{s}_0$ in the reference configuration; and the strain anisotropic invariants are defined as: $I_{4f} = \mathbf{f}_0 \otimes \mathbf{C}\mathbf{f}_0 = C_{ij} f_{0i} f_{0j}$, $I_{4s} = \mathbf{s}_0 \otimes \mathbf{C}\mathbf{s}_0 = C_{ij} s_{0i} s_{0j}$, $I_{8fs} = \mathbf{f}_0 \otimes \mathbf{C}\mathbf{s}_0 = C_{ij} f_{0i} s_{0j}$, with summation $i$,$j$=1,2,3. The material constants were determined from biaxial experiments and shear of tissue samples loaded in the myocardium sheet plane, for porcine and human tissue. Besides measurements for determining the material constants, compression tests were performed to evaluate the compressibility constitutive relationship. The computed results using the model defined by equations (5) and (6) agreed very well with experiments.

## 2. Computational procedure using directly the constitutive curves

In the previous section, we presented typical formulations of constitutive laws where the adopted relationships include material constants that have to be determined from the corresponding experiments. That two-steps approach consists of: (1) formulation of a basic analytical form based on fundamental physical laws, and (2) fitting material parameters to match prediction by the model and experimental finding. Motivation for our "direct" use of the measured relationships is to avoid these two steps, i.e. to include the constitutive curves directly into the finite element models.

We first introduce the basic geometry of the ventricle wall and experimental constitutive relationships, then summarize the fundamental relations from continuum mechanics and the relevant expressions of the finite element methodology, and finally present details of our computational procedure.

### *2.1 Characteristics of deformation of the left ventricle*

Two distinct regimes are repeated over heart cycles: systole and diastole. During systole, the left and the right ventricles contract pumping blood from the heart: to the arterial system from the left ventricle (LV) and to the lung from the right ventricle (RV). The atria expand so that the blood comes from veins (right atrium) and from the lung (left atrium). During diastole, the atria contract, and blood flows from atria into ventricles that expand. This expansion is produced by loading coming from the blood entering the ventricles. Maximum deformation and therefore maximum (passive) stress within the tissue of ventricles occurs at the end of diastole. During systole, the active stress is generated within muscle cells and, together with the passive stress, provides the mechanical forces to overcome the resistance to blood flow into the arterial system (from LV) and into the lung (from RV). The resistance to blood flow to the arterial system is higher than to the lung, therefore the overall loading is higher on the walls of the LV. Due to these circumstances, a study of processes in the LV is of primary interest. Heart dysfunction deceases, and heart failure are often related to the tissue of the left ventricle. Mechanical characteristics of

the LV tissue represent one of the fundamental components of heart behavior and have been under investigation over centuries.

Morphology of the left ventricle tissue is very complex. The microstructural composition has been intensively studied and it has been described in medical and engineering literature (i.e. Sommer et al., 2015; Holzapfel and Ogden, 2009; McEvoy et al., 2018). We here outline the specificities that are the most important for our computational modeling. Fig. 1A shows a schematic of the ventricle according to (Bovendeerd et al., 1992), indicating that geometrically the ventricle can be approximated by a thick shell. The wall is composed of layers (or sheets) of parallel muscle cells (myocytes) which has a fibrous character and occupying about 70 % of the volume. The remaining 30 % consists of various interstitial components, where 2-5 % represent collagen network for lateral connections. Long muscle cells form fibers where the muscle activation occurs producing active stress along directions of fibers. The material can be considered orthotropic with the orthotropic unit vectors **f** and **s** for the fiber and sheet directions, respectively, lying in the tangential plane of the sheet surface. The third direction is defined by the unit vector **n** normal to the sheet plane, as shown in Fig. 1A. As stated above, the fibers have helicoidal character with the angle $\phi$ changing over the wall thickness.

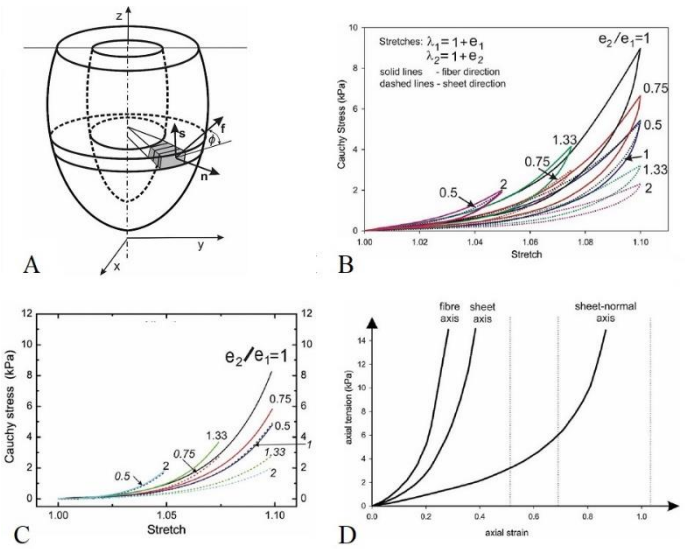


**Fig. 1.** (A) Schematic of the geometry of the left ventricle with material element and local unit vectors of fiber, sheet, and normal directions; (B) Average constitutive curves (26 samples) for human left ventricle tissue subjected to biaxial loading for various ratios of sheet strain e2 and fiber strain e1, according to (Sommer et al., 2015); (C) Average constitutive curves for human left ventricle tissue subjected to biaxial loading, with mean values of the loading and unloading, and for several ratios of sheet strain e2 and fiber strain e1, according to (Sommer et al., 2015); (D) Constitutive curves obtained by uniaxial tension in the three material directions of the left ventricle tissue of pig, according to (Stevens et al., 2003).

**Biaxial tests.** The mechanical behavior of the ventricle as a thick shell structure is mainly characterized by the mechanical properties of the sheet layers. Due to these circumstances, experimental and theoretical investigations are focused on the kinematics of deformation and constitutive laws of the sheet layers, as outlined in the Introduction. Mechanical investigations are usually performed as biaxial loading and shear on a sample in a sheet plane. Fig. 1B shows average constitutive curves obtained by using samples of 26 human ventricles subjected to biaxial

loading in the sheet plane. Tests were performed by loading and unloading into fiber (MFD – according to notation in (Sommer et al., 2015)) and sheet (CFD) directions up to three levels of maximum stretch (1.05, 1.075,1.1) and maintaining the constant ratios between strain $e_2 = \lambda_2 - 1$ in the sheet direction and fiber strain $e_1 = \lambda_1 - 1$; here $\lambda_2$ and $\lambda_1$ are stretches. It can be seen that the constitutive curves are highly nonlinear, with hyper-elastic characteristics common for biological materials. The stress-stretch relationship depends on the stretch level to which the material is stretched before unloading and on the stretch ratio. The material displays hysteretic character, with hysteresis that leads to energy dissipation, more pronounced at a higher level of stretch. Fig. 1C shows average constitutive curves with the curves obtained using mean values of the loading and unloading paths. They can be used in our computational procedure and in applications of the analytical forms of the constitutive laws (some of these forms are given in Section 1).

We here add constitutive curves for the left ventricle of pig according to (Stevens et al., 2003), Fig. 4. These curves include the stress-strain relationship for the sheet-normal direction which will be used in our computational model. The analytical form (3) of deformation energy was used in (Stevens et al., 2003) with the fitting of material constants according to the graphs in Fig. 1D.

**Shear tests.** In reference (Sommer et al. 2015) are reported results of triaxial shear tests. Six modes of shear deformation are generated, in planes corresponding to the f-s-n material coordinate system of the undeformed material, with initial unit vectors $\mathbf{f}_0,\mathbf{s}_0,\mathbf{n}_0$ shown in Fig. 2A. Shear stresses corresponding to each mode are expressed in terms of the 'amount of shear' $\Delta L / L$ where $\Delta L$ is displacement in direction of the shear stress and L is the sample dimension. This amount of shear represents a part of the usually used engineering shear strain of a continuum. The specimen was loaded in cycles, where loading is increased and then decreased, further followed by loading in the opposite direction. Also, tests were performed with different load levels. Results shown in Figs. 2B, 2C and 2D display anisotropic and hysteretic character of the material under shear. The shear stresses are the largest on planes with normal f (FS and FN) and smallest on planes with normal n (NF and NS).

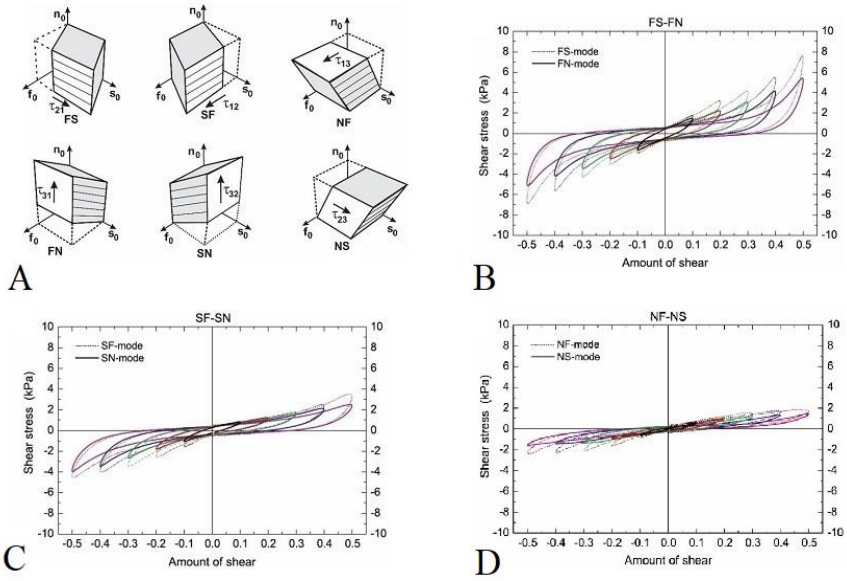


**Fig. 2.** (A) Shear modes used in triaxial shear tests (Sommer et al., 2015); Shear constitutive curves, the relation between shear stress and amount of shear, for the six planes: (B) FS-FN, (C) SF-SN and (D) NF-NS according to (Sommer et al., 2015).

*2.2 Fundamental continuum and finite element relations*

Here are summarized the basic relations further used in the computational procedure. We will use, for clarity of the presentation, both direct and indicial notation where is appropriate. The fundamental quantity for the description of the kinematics of deformation is deformation gradient (general 3D conditions are assumed),

$$ {}^{t}_{0}\mathbf{F} = \frac{\partial {}^{t}\mathbf{x}}{\partial {}^{0}\mathbf{x}} = \mathbf{I} + \frac{\partial {}^{t}\mathbf{u}}{\partial {}^{0}\mathbf{x}}, \quad \text{or} \qquad {}^{t}_{0}F_{ij} = \frac{\partial {}^{t}x_i}{\partial {}^{0}x_j} = \delta_{ij} + \frac{\partial {}^{t}u_i}{\partial {}^{0}x_j} \tag{8} $$

where and ${}^{0}\mathbf{x}$ and ${}^{t}\mathbf{x}$ are position vectors of a material point in the initial (reference) ${}^{0}$□ and current ${}^{t}$□ configuration (time t), respectively; ${}^{t}\mathbf{u}$ is displacement in the coordinate system $x_i$, i=1,2,3 and $\delta_{ij}$ is the Kronecker delta symbol. The following relations will be further used (Kojic and Bathe, 2005),

$$ {}^{t}_{0}\lambda = \left| {}^{t}_{0}\mathbf{F}\,{}^{0}\mathbf{n} \right| \tag{9} $$

$$ {}^{t}\mathbf{n} = \frac{1}{{}^{t}_{0}\lambda}\,{}^{t}_{0}\mathbf{F}\,{}^{0}\mathbf{n} \tag{10} $$

where ${}^{t}_{0}\lambda$ is a stretch of material in direction of the unit vector ${}^{t}\mathbf{n}$, in the initial configuration ${}^{0}\mathbf{n}$. If the finite element (FE) discretization is employed, the position and displacement vectors are expressed as:

$$ x_i = N_I X_i^I, \quad sum\ on\ I\text{: } I = 1,2,...,\ N \tag{11} $$

$$ {}^{t}u_i = N_I \, {}^{t}U_i^I, \quad sum\ on\ I: I = 1,2,..., N \tag{12} $$

where N is the number of FE nodes; $X_i^I$ and are FE nodal point coordinates (in a specified configuration), and ${}^{t}U_i^I$ are nodal point displacements. The deformation gradient can be expressed as

$$ {}_0^t\mathbf{F} = {}^{t}\mathbf{J} \, {}^{0}\mathbf{J}^{-1} \tag{13} $$

where

$$ {}^{0}J_{kj} = \frac{\partial {}^{0}x_k}{\partial r_j} = \frac{\partial N_I}{\partial r_j} \, {}^{0}X_k^I, \quad {}^{t}J_{kj} = \frac{\partial {}^{t}x_k}{\partial r_j} = \frac{\partial N_I}{\partial r_j} \, {}^{t}X_k^I \qquad sum\ on\ I \tag{14} $$

are Jacobian matrices of transformation between Cartesian $x_i$ and natural coordinates $r_i$.

We use usual definitions of small normal strain components needed for the FE formulation since the relations for small strains are applicable to the virtual strains,

$$ \mathbf{e}^{(3)} = \mathbf{B}^{(3)}\mathbf{U} \tag{15} $$

where

$$ e_1^{(3)} = \frac{\partial u_1}{\partial x_1}, \; e_2^{(3)} = \frac{\partial u_2}{\partial x_2}, \; e_3^{(3)} = \frac{\partial u_3}{\partial x_3} \tag{16} $$

and $\mathbf{B}^{(3)}$ represents the first three rows in a FE standard formulation of the strain-displacement matrix **B** (Kojic et al., 2008), and **U** is the finite element displacement vector. These strains can be transformed to the local f,s,n (further also denoted as $\bar{x}_1 \equiv f$, $\bar{x}_2 \equiv s$, $\bar{x}_3 \equiv n$) material system by using the transformation matrix for strains $\mathbf{T}^{\varepsilon}$ (Kojic et al., 2008) which contains directional cosines between $x_i$ and $\bar{x}_i$ coordinate axes:

$$ \bar{\mathbf{B}}^{(3)} = \mathbf{T}^{\varepsilon T}\mathbf{B}^{(3)} \tag{17} $$

$$ \bar{\mathbf{e}}^{(3)} = \bar{\mathbf{B}}^{(3)}\mathbf{U} \tag{18} $$

For the shear components we use amount of shear defined as

$$ e_{ij} = \frac{\partial u_i}{\partial x_j}, \quad i \neq j, \; i, j = 1,2,3 \tag{19} $$

or in the matrix form

$$ \mathbf{e}^{shT} = \left[ \frac{\partial u_1}{\partial x_2} \frac{\partial u_2}{\partial x_1} \frac{\partial u_2}{\partial x_3} \frac{\partial u_3}{\partial x_2} \frac{\partial u_1}{\partial x_3} \frac{\partial u_3}{\partial x_1} \right] \tag{20} $$

We can transform these strains into the local material system by a matrix transformation:

$$ \frac{\partial \bar{u}_i}{\partial \bar{x}_j} = T_{im} T_{jk} \frac{\partial u_m}{\partial x_k}, \quad i \neq j; \; sum\ on\ m\ and\ k: \; m,k = 1,2,3 \tag{21} $$

where $T_{im} = \cos\left(\bar{x}_i, x_m\right)$ is the matrix of the directional cosines. Therefore, we can further write

$$\frac{\partial \bar{u}_i}{\partial \bar{x}_j} = T_{im} T_{jk} \frac{\partial N_I}{\partial x_k} U_m^I \tag{22}$$

This relation can be written in the direct notation as

$$\bar{\mathbf{e}}^{sh} = \bar{\mathbf{B}}^{sh} \mathbf{U} \tag{23}$$

where the matrix $\bar{\mathbf{B}}^{sh}$, with dimensions 6x3N, follows from relations (22). The shear strain matrix $\bar{\mathbf{e}}^{sh}$ is

$$\bar{\mathbf{e}}^{shT} = \left[ \frac{\partial \bar{u}_1}{\partial \bar{x}_2} \frac{\partial \bar{u}_2}{\partial \bar{x}_1} \frac{\partial \bar{u}_2}{\partial \bar{x}_3} \frac{\partial \bar{u}_3}{\partial \bar{x}_2} \frac{\partial \bar{u}_1}{\partial \bar{x}_3} \frac{\partial \bar{u}_3}{\partial \bar{x}_1} \right] \tag{24}$$

Combining (18) and (23) we obtain

$$\bar{\mathbf{e}} = \begin{bmatrix} \bar{\mathbf{e}}^{(3)} \\ \bar{\mathbf{e}}^{sh} \end{bmatrix} = \begin{bmatrix} \bar{\mathbf{B}}^{(3)} \\ \bar{\mathbf{B}}^{sh} \end{bmatrix} \mathbf{U} = \bar{\mathbf{B}} \mathbf{U} \tag{25}$$

where $\bar{\mathbf{B}}$ is 9x3N matrix accounting for all nine strain components.

The 9x1stress matrix with the work-conjugate components to the above 9 strains is:

$$\bar{\boldsymbol{\sigma}}^T = \left[ \sigma_{ff} \sigma_{ss} \sigma_{nn} \tau_{sf} \tau_{fs} \tau_{ns} \tau_{sn} \tau_{nf} \tau_{fn} \right] \tag{26}$$

where notation $\sigma$ is used for normal and $\tau$ for shear stresses.

Using velocities as nodal variables, which are more appropriate for coupling motion of the heart wall with blood flow, the incremental-iterative equations of the force-balance for a finite element and per unit volume can be written in a usual form (Kojic et al., 2008),

$$\left( \frac{1}{\Delta t} \mathbf{M} + \bar{\mathbf{K}}^{(i-1)} \right) \Delta \mathbf{V}^{(i)} = \mathbf{F}^{ext(i)} - \mathbf{F}^{\text{int}(i-1)} - \frac{1}{\Delta t} \mathbf{M} \left( \mathbf{V}^{(i-1)} - \mathbf{V}^t \right) \tag{27}$$

where $\Delta t$ is time step, i is iteration counter and $\mathbf{F}^{ext(i)}$ are external nodal forces acting on the element; $\mathbf{V}^{(i-1)}$ and $\mathbf{V}^t$ are nodal velocities at previous iteration and at start of the time step, respectively. The mass and stiffness matrix are:

$$\mathbf{M} = \rho \mathbf{N}^T \mathbf{N}, \quad \bar{\mathbf{K}}^{(i-1)} = \left( \bar{\mathbf{B}}^T \mathbf{C}_T \bar{\mathbf{B}} \right)^{(i-1)} \tag{28}$$

where $\rho$ is mass density, and vector of the internal nodal forces is

$$\mathbf{F}^{\text{int}(i-1)} = \bar{\mathbf{B}}^{T(i-1)} \bar{\boldsymbol{\sigma}}^{(i-1)} \tag{29}$$

The tangent constitutive matrix $\mathbf{C}_T^{(i-1)}$ in the local system will be determined within the computational procedure presented in the next section.

*2.3 Computational procedure for stress calculation*

In the displacement-based FE modeling, the increments of displacements (velocities) are calculated at each iteration by solving the balance equations of the FE assemblage. The convergence criteria are implemented and, if they are not satisfied, the calculation of stresses and nodal forces is repeated. In this process, a key segment is the evaluation of stresses, which in the FE literature is usually called stress integration (Kojic and Bathe, 2005), (Bathe, 1996). Stresses are evaluated at each integration point according to constitutive relationships and the current values of the quantities describing the kinematics of deformation. Here, these quantities are stretches in the three local directions and the 'amount of shear' in the local fiber-sheet-normal system. There are several issues to be resolved in the computational procedure for the proposed model:

a) Calculation of stresses based on the constitutive curves;

b) Calculation of the tangent constitutive matrix;

c) Formulation of methodology for coupling the local stresses.

*a) Calculation of stresses*

Consider first normal stresses. We use experimental curves given in Fig. 1B. The concept of determination of normal stresses is displayed in Fig. 3 for the loading regime. For the current iteration (here is omitted iteration counter *i*), we calculate the stretches $\lambda_1$ and $\lambda_2$ from (9) for the fiber direction **f** and sheet direction **s**, respectively. Therefore, we have the ratio between strains $e_2 = |\lambda_2 - 1|$ and $e_1 = |\lambda_1 - 1|$, $c = e_2 / e_1$. Consider first sheet direction, Fig. 3A. If the ratio is between experimental curves with ratios *a* and *b*, i. e. $c \geq a,\ \mathrm{c} \leq \mathrm{b}$ then we have the linearly interpolated stress $\bar{\sigma}_A$ as

$$\bar{\sigma}_A = \frac{c-a}{b-a}\left(\bar{\sigma}^2 - \bar{\sigma}^1\right) \tag{30}$$

where $\bar{\sigma}^1$ and $\bar{\sigma}^2$ are stresses at the lower and upper curves, respectively. In case when $e_2 / e_1 < a_{\min}$ we use interpolation

$$\bar{\sigma}_B = \frac{c}{a_{\min}}\bar{\sigma}^1 \tag{31}$$

and when $e_2 / e_1 > a_{\max}$ the interpolation is:

$$\bar{\sigma}_C = \bar{\sigma}^2 + \left(\frac{c}{a_{\max}} - 1\right)\bar{\sigma}^2 = \frac{c}{a_{\max}}\bar{\sigma}^2 \tag{32}$$

Constitutive curves for sheet direction are shown in Fig. 3B, with the opposite interpolation along the stress-axis with respect to Fig. 3A.

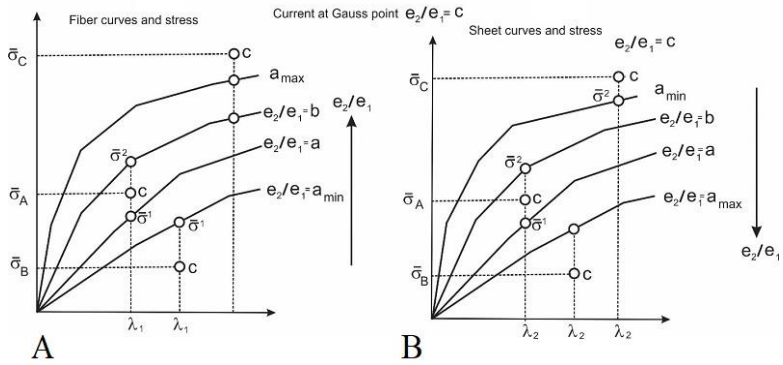


**Fig. 3.** Interpolation of normal stresses in the local (material) coordinate system, loading regime. (A) Fiber direction; (B) Sheet direction.

The tangent modulus is related to stress increment with respect to the strain increment in the local system and is calculated as

$$\bar{E}_{T1} = \lambda_1 \frac{\partial \bar{\sigma}_1}{\partial \lambda_1} = \lambda_1 E_{T1}^{\lambda}, \quad \bar{E}_{T2} = \lambda_2 \frac{\partial \bar{\sigma}_2}{\partial \lambda_2} = \lambda_2 E_{T2}^{\lambda} \tag{33}$$

where $E_{T1}^{\lambda}$ and $E_{T2}^{\lambda}$ are interpolated tangent moduli on the experimental constitutive curves. Interpolation goes over different curves and three load levels, initially starting with level 1.

For the normal direction, we use the sheet experimental curves from Fig. 1B and implement scaling factors for strains according to the difference between the sheet-normal and sheet curves of (Stevens et al., 2003), Fig.4.

Shear stresses are determined by interpolation over experimental shear curves for each of the six shear components. The interpolation is analogous to that shown for normal components, but it is simpler since the shear components are mutually independent and we follow one curve for each component during the loading and unloading regime.

The unloading starts from the stress-strain point reached during loading, in case of normal and shear stresses. We will show this concept in the numerical examples in Section 3.

*b) Tangent constitutive matrix*

The constitutive matrix **C** is a diagonal matrix,

$$C_{ii} = \bar{E}_{Ti}, \quad i = 1,2,3; \qquad C_{ii} = \bar{G}_{Ti}, \quad i = 4,5,..,9 \tag{34}$$

where $\bar{E}_{Ti}$ are tangent moduli for normal components according to (33) and $\bar{G}_{Ti}$ are tangent shear moduli. The tangent moduli are evaluated from the experimental curves in Figs. 1B and 2B.

*c) Coupling the local stresses*

The above-calculated stresses and constitutive matrix **C** lead to a decoupled response, i.e. loading in one material direction would not produce deformation in the other two material directions. This is not in agreement with the obvious physiological observation and experiments shown in Fig. 1B. Also, the dominant normal stresses in the sheet plane of the heart wall produce a change of the wall thickness. The material also displays compressibility with volumetric strain even of the

order of several percent (McEvoy et al. 2018). We have used a penalty method for incompressible conditions and introduced a novel formulation for compressible material behavior.

The penalty method for incompressible material is based on the relation for a constraint $W_{constr}$, (Bathe, 2005),

$$W_{constr} = \frac{1}{2}\lambda_p \int_V \left( \frac{\partial v_i}{\partial x_i} \right)^2 dV, \quad sum\ on\ i \tag{35}$$

where $\lambda_p$ is a penalty parameter and the integration is performed over the finite element volume $V$. The variational form of this integral is equal to zero,

$$\delta W_{constr} = \delta v_i \lambda_p \int_V v_{j,j} dV = \delta V_i^I \lambda_p \int_V \left( N_{I,j} N_{J,j} dV \right) V_j^J = \delta V_i^I \lambda_p K_{IiJj}^{\lambda} V_j^J = 0, \quad sum\ on\ j \tag{36}$$

where $K_{IiJj}^{\lambda}$ is the penalty matrix added to other element matrices.

In the case of compressible conditions, we first split deformation energy into a deviatoric part, which is associated with shape deformation, and a volumetric part associated with the volume change (analogous to elastic-plastic models, (Kojic and Bathe, 2005)). Hence, we define deviatoric strains $e_i'$ (with the one-index notation and in the local f-s-n coordinate system) as

$$e_i' = \bar{e}_i - e_m, \quad i = 1,2,3; \quad e' = \bar{e}_i, \quad i = 4,5,...9 \tag{37}$$

where $e_m = \left( e_{11} + e_{22} + e_{33} \right) / 3 = e_V / 3$ is the mean strain and $e_V$ is volumetric strain. The deviatoric stresses $\sigma_i'$ are defined as

$$\sigma_i' = \bar{\sigma}_i - \sigma_m, \quad i = 1,2,3; \qquad \sigma_i' = \bar{\sigma}_i, \quad i = 4,5,...9 \tag{38}$$

where $\sigma_m = \left( \sigma_{11} + \sigma_{22} + \sigma_{33} \right)$ is the mean stress. Virtual work can be expressed as

$$\delta W = \bar{\sigma}_i \delta \bar{e}_i = \sigma_i' \delta e_i' + \delta e_V \sigma_m = \delta \tilde{e}_j \tilde{\sigma}_j, \quad i = 1,2,..,9; \; j = 1,2,...,10 \tag{39}$$

where the mean strain and mean stress are included as additional variables, i.e,

$$\tilde{\mathbf{e}}^T = \left[ e_1', e_2', e_3', e_{12}, e_{21}, .., e_{31}, e_V \right], \qquad \tilde{\boldsymbol{\sigma}}^T = \left[ \sigma_1', \sigma_2', \sigma_3', \tau_{21}, \tau_{12}, .., \tau_{13}, \sigma_m \right] \tag{40}$$

The strains can be expressed as

$$\tilde{\mathbf{e}} = \begin{bmatrix} \mathbf{e}' \\ e_V \end{bmatrix} = \begin{bmatrix} \mathbf{B}' \\ \mathbf{B}^m \end{bmatrix} \mathbf{U} = \tilde{\mathbf{B}} \mathbf{U} \tag{41}$$

where submatrices $\mathbf{B}'$ and $\mathbf{B}^m$ can be expressed by the matrix $\bar{\mathbf{B}}$ the local system as follows. For node $I$ the terms of the matrix $\mathbf{B}'$ are

$$
\begin{aligned}
B'^{I}_{1,(3I-2)} &= \frac{2}{3}B^{I}_{1,(3I-2)} - \frac{1}{3}B^{I}_{2,(3I-2)} - \frac{1}{3}B^{I}_{3,(3I-2)} \\
B'^{I}_{1,(3I-1)} &= \frac{2}{3}B^{I}_{1,(3I-1)} - \frac{1}{3}B^{I}_{2,(3I-1)} - \frac{1}{3}B^{I}_{3,(3I-1)} \\
B'^{I}_{1,3I} &= \frac{2}{3}B^{I}_{1,3I} - \frac{1}{3}B^{I}_{2,3I} - \frac{1}{3}B^{I}_{3,3I} \\
B'^{I}_{2,(3I-2)} &= -\frac{1}{3}B^{I}_{1,(3I-2)} + \frac{2}{3}B^{I}_{2,(3I-2)} - \frac{1}{3}B^{I}_{3,(3I-2)} \\
B'^{I}_{2,(3I-1)} &= -\frac{1}{3}B^{I}_{1,(3I-1)} + \frac{2}{3}B^{I}_{2,(3I-1)} - \frac{1}{3}B^{I}_{3,(3I-1)} \\
B'^{I}_{2,3I} &= -\frac{1}{3}B^{I}_{1,3I} + \frac{2}{3}B^{I}_{2,3I} - \frac{1}{3}B^{I}_{3,3I} \\
B'^{I}_{3,(3I-2)} &= -\frac{1}{3}B^{I}_{1,(3I-2)} - \frac{1}{3}B^{I}_{2,(3I-2)} + \frac{2}{3}B^{I}_{3,(3I-2)} \\
B'^{I}_{2,(3I-1)} &= -\frac{1}{3}B^{I}_{1,(3I-1)} - \frac{1}{3}B^{I}_{2,(3I-1)} + \frac{2}{3}B^{I}_{3,(3I-1)} \\
B'^{I}_{2,3I} &= -\frac{1}{3}B^{I}_{1,3I} - \frac{1}{3}B^{I}_{2,3I} + \frac{2}{3}B^{I}_{3,3I}
\end{aligned}
\tag{42}
$$

where the subindices 1,2,3 are related to the directions 1,2,3 of the node. For matrix $\mathbf{B}^{m}$ we have

$$B^{mI}_{k} = B^{I}_{1k} + B^{I}_{2k} + B^{I}_{3k},\ k = 1,2,3 \tag{43}$$

The deviatoric stresses follow from stresses determined from the experimental Holzapfel curves. The mean stress is determined from a compressibility curve as given in (McEvoy et al., 2018), Fig. 4.

$$\sigma^{c}_{m} = \sigma_{m}\left(e_{V}\right) \tag{44}$$

The bulk modulus is evaluated from the compressibility curve as

$$K_{V} = \frac{\partial \sigma_{m}\left(e_{V}\right)}{\partial e_{V}} \tag{45}$$

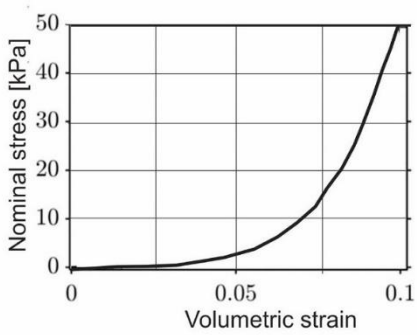


**Fig. 4.** Experimentally determined dependence of the compressive stress on the volumetric strain, according to (McEvoy et al., 2018).

The form (28) for stiffness matrix has now different expressions for terms corresponding to normal stresses and strains, and also has additional terms for the volumetric part. For the normal components, we have

$$\tilde{K}_{ilkJ} = B'_{iI} C_{ik} \bar{B}_{kJ}, \quad i,k = 1,2,3; \quad I,J = 1,2,....,N \tag{46}$$

where indices *i* and *k* indicate relative positions of a term for nodes *I* and *J*, respectively. Further,

$$\begin{aligned} &C_{ii} = \frac{2}{3}\bar{E}_{Ti}, \quad i = 1,2,3; \quad \textit{no sum on } i \\ &C_{21} = C_{31} = -\frac{1}{3}\bar{E}_{T1}, \quad C_{12} = C_{32} = -\frac{1}{3}\bar{E}_{T2}, \quad C_{13} = C_{23} = -\frac{1}{3}\bar{E}_{T3} \end{aligned} \tag{47}$$

The shear part of the matrix **C** is diagonal: shear terms are as in equation (34), while the term relating to the mean stress and volumetric strain is

$$C_{10,10} = K_V \tag{48}$$

where $K_V$ is compressibility modulus. In case of incompressibility, a large number of the modulus can be used.

## 3. Verification of the computational procedure

In this section, we present numerical examples using one 3D finite element subjected to various loading conditions to verify the proposed numerical procedure and then implement the model to the left ventricle deformation. The correctness of this procedure relies on the satisfaction of the following conditions:

a) The experimental curves for biaxial loading and shear should be followed;

b) The compressibility relationship should be satisfied.

Besides these requirements, we will demonstrate how interpolation between experimental constitutive curves affects the solutions.

### *3.1 Example 1 – prescribed stretches in biaxial loading*

Numerical results are obtained with simple 3D element with prescribed displacement in *x* and *y* directions (Fig. 5A) in order to keep unchanged the selected ratio of strains over the entire cycle. Results are shown for three different ratios of the strains between sheet direction (CFD), e2, and fiber direction (MFD), e1. The solutions are obtained using penalty formulation, equation (36) (denoted as 'Penalty' in the figures); and using a formulation with compressibility and strain decomposition according to equations (37) and (38) (denoted as 'deviatoric'), with compressibility modulus $K_V$=10kPa which provides incompressibility. We examined $e_2/e_1 = 1$, $e_2/e_1 = 2$ and $e_2/e_1 = 0.625$. Examples $e_2/e_1 = 1$ and $e_2/e_1 = 2$ show that numerical results follow experimental curves, while the case $e_2/e_1 = 0.625$ demonstrates the interpolation between two experimental curves $e_2/e_1$=0.5 and $e_2/e_1$=0.75. All examples have prescribed a maximum stretch of 1.1. Experimental curves of level 3 in Fig. 1B are taken here, so that there is no 'jump' due to passing from lower level to the higher; use of multiple levels is shown for shear deformation, in Example 3.

We further present one example to demonstrate that the numerical solution agrees with the compressibility curve from Fig. 4. The results are obtained for $e_2/e_1 = 1$ and assuming a symmetric cycle with a maximum prescribed displacement of 0.3, Fig. 6A. In Fig. 6B) is shown a relative change of the wall thickness (displacement in the z-direction in Fig. 5A).

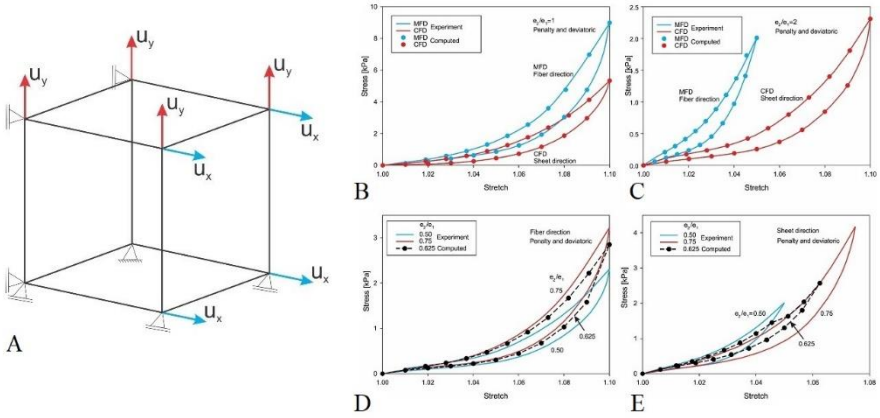


**Fig. 5.** (A) A 3D finite element with prescribed displacements used to model the stretch of the material. Fibers are aligned with x-direction (MFD), and axes y and z correspond to sheet (CFD) and normal directions, respectively. Dimensions of the element are equal to unity; Computed and experimental stress-stretch curves. Loading and unloading for strain ratios e2/e1 = 1 (B) and e2/e1 =2 (C) used in experiments; Interpolation of the constitutive relation between adjacent curves for strain ratio e2/e1=0.625: (D) for fiber direction and (E) for sheet direction.

From the results shown in Figs. 5B and 6, it can be seen that the numerical procedure implemented in the code PAK-BIO (Kojic et al., 2018) provides a good agreement with the measured constitutive curves.

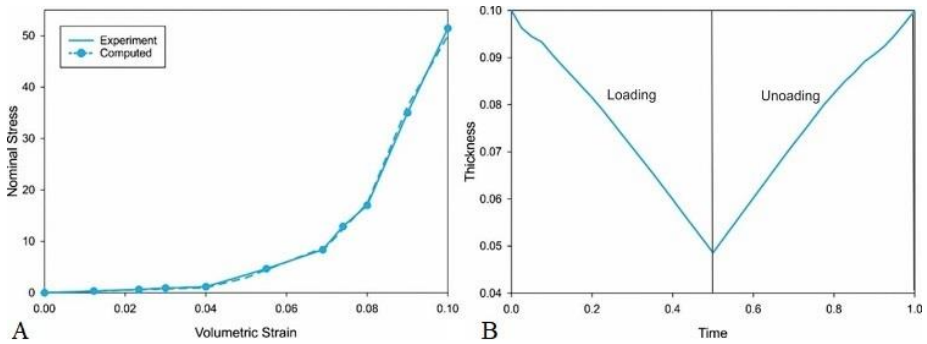


**Fig. 6.** Biaxial stretch with the strain ratio e2/e1=1, symmetric cycle. Time is a loading parameter (inertial forces are neglected). (A) Relation between nominal (tension) stress and volumetric strain; (B) Computed wall thickness over the cycle.

*3.2 Example 2 – prescribed stretches in biaxial loading with 75% of a max stretch from the experimental curve*

Here we consider the case $e_2/e_1 = 2$ as in Fig. 5C, but with the maximum stretches reaching 75% of the maximum on the experimental curve. Then, in the reverse loading, we calculate hysteresis by an algorithm where we scale the experimentally measured hysteresis. The scaling factor is defined as the ratio between the maximum stretch $\lambda_{\max}$ reached in the loading regime within a cycle, and the maximum stretch on the corresponding experimental curves $\lambda_{\max}^{\exp}$. The computed constitutive relationship with the reduced hysteresis is shown in Fig. 7.

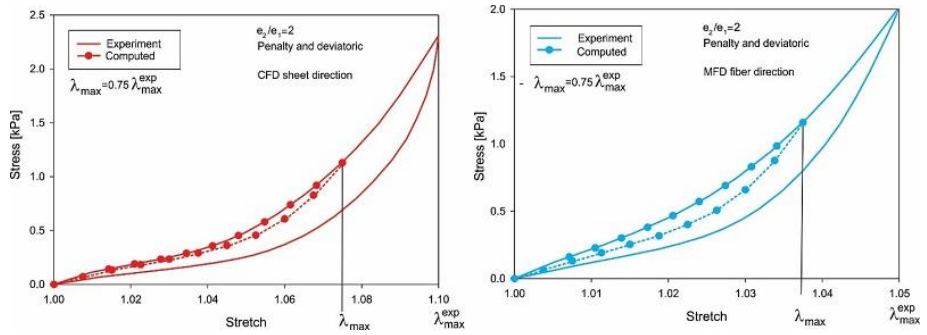


**Fig. 7.** Computed constitutive relations in case of reduced hysteresis (scaling factor is $\lambda_{\max}/\lambda_{\max}^{\exp}$ ).

*3.3 Example 3 – shear loading*

Here, we prescribe displacements to generate shear conditions as FS mode in Fig. 2A. Experimental curves are obtained for different values of the maximum shear. There are 5 levels: 0.1, 0.2, 0.3, 0.4 and 0.5. We increase shear from zero to a maximum value of 0.5 and the stresses are obtained as follows. We start with using the curve of level 1 until the maximum value of 0.1 is reached and then continue on the curve on level 2, and so on. A change of the level produces discontinuity (a jump) as shown in the figure. The reverse loading follows the unloading curve of the last level reached in the loading regime and with a scaling factor as in the case of stretches described above and shown in Fig. 9B). In practical application to heart cycles, we keep the strain

level for a current cycle for each integration point (or node) and start the next cycle with the last levels and update by new levels. Cycles are repeated until there is no change of strain levels – therefore, the reached levels are relevant to model the heart mechanics. This concept is implemented into our code PAK-BIO (Kojic et al., 2018) for stretch and shear constitutive curves.

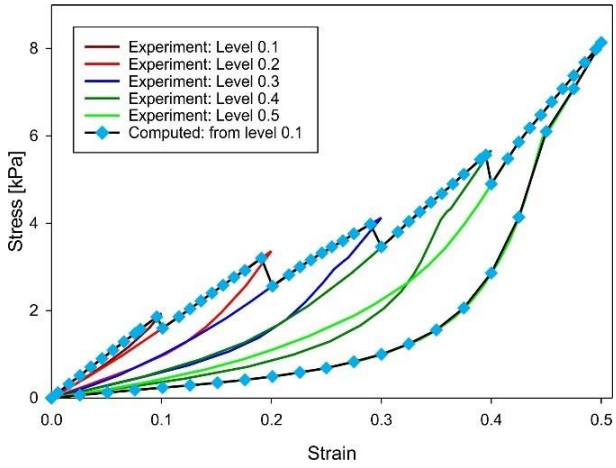


**Fig. 8.** Numerical results for shear if all 5 levels of experimental curves are reached.

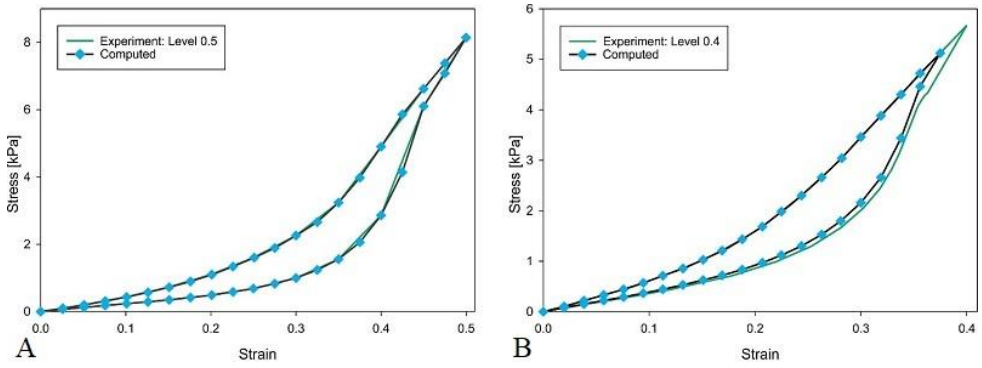


**Fig. 9.** Numerical results for shear in the case when one curve is used. (A) Maximum experimental value of shear is reached; (B) Maximum shear is not reached.

## 4. Application to left ventricle model generated from the echocardiogram

Here we implement the developed computational procedure for modeling of cardiac tissue to real physiological conditions of the left ventricle. The FE model, generated from the echocardiogram recorded in a clinic, provides an insight into the mechanics of the LV during a cardiac cycle.

The transthoracic echocardiogram of a healthy 38-years old mail was recorded at the Cardiology Department, University Clinical Center of Serbia, Belgrade, according to the current guidelines in (Lang et al., 2015), using a Vivid E95 ultrasound system (General Electric Vingmed Ultrasound, Milwaukee, WI) with patients at rest in the left lateral decubitus position. Electrocardiogram-triggered echocardiographic data were acquired with M5 transducers and

digitally stored in a cine-loop format (3 cardiac cycles, 60 fps). Apical views were used to acquire 2-dimensional data. The recorded cardiograms were used in the following way.
Three planes fixed in space, at angles 90°, 150°, and 210°, are used and the geometry of the LV inner surface for selected times is generated in a semi-automatic manner. We perform the following basic steps:

1) Extraction of contours with a specification of dimensions of the configuration;
2) Fitting of contours within planes at angles 90°, 150°, and 210° in 3D space;
3) Use of splines and linear interpolation to determine positions of the points at the surface;
4) Generation of faces from the points of the model;
5) Finite elements mesh generation of the wall tissue at the initial configuration;
6) Generation of fibers at the initial configuration.

These steps are illustrated in Fig. 10. Steps 1-4 are repeated for all configurations. We generate finite element mesh and fiber directions only for initial configuration. The generated fibers are helicoidal with an angle varying from -60° at epicardium to 60° at endocardium, with respect to the sheet (circumferential) direction.

In this procedure of the generation of the FE mesh on the surface, we keep the number of points fixed. However, the goal is to generate the points which represent the same material points during the internal LV surface motion. In order to achieve this, we include rotation of the LV (Salem Omar et al., 2015) and the correct position of each point. As shown in Fig. 11A, we assume linear distribution of rotation along the axial axis. Therefore, for each point, we have the rotation angle over time.

The 3D FE model of the LV wall is generated from the geometry of the inner surface in the following way. We start with the stress-free configuration of the wall tissue that corresponds to the start of diastole (minimum volume configuration). In that initial configuration, we assign wall thicknesses to each of the FE nodes using the geometry of the external surface from the echocardiogram and establish the initial 3D finite element mesh. Also, we generate the initial fiber directions, as in Fig. 10. Selecting a time step, we generate the internal surface geometry at end of the time step, impose displacements at the inner surface, and solve for displacements of other FE points of the LV wall. Here we use constitutive relations and numerical procedure for stress calculation according to Section 2.

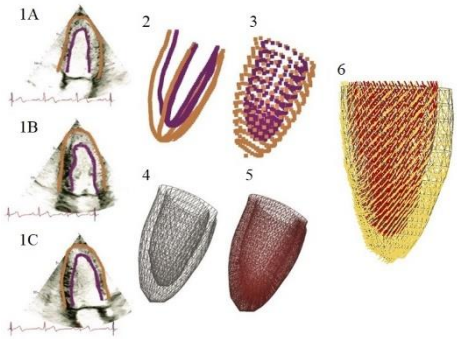


**Fig. 10.** Left ventricle model generation from the echocardiogram. Steps 1A, 1B, and 1C: extraction of contours in planes at angles 90°, 150°, and 210° respectively; step 2: fitting of contours into 3D space; step 3: generation of points at the epicardium and endocardium; step 4: generation of faces; step 5: finite element mesh generation for the wall tissue at initial configuration; step 6: generation of fibers at initial configuration.

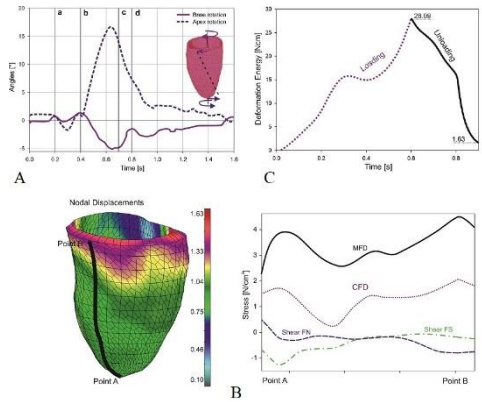


**Fig. 11.** (A) Rotation angles of the base and apex of the LV during a cycle, and linear interpolation over the LV axial axis (Salem Omar et al., 2015); (B) Displacement field and stress distribution along a line AB on the wall surface at time t=0.6s (end of diastole); (C) Deformation energy for the LV wall tissue over a heart cycle, Maximum energy is ME=28.02 and hysteretic energy is HE= 2.57; the HE is approximately 9% of the ME.

Fig. 11B shows displacement field and stresses along a selected line on the external wall at the end of diastole, i.e. when the volume of the LV reaches maximum. It can be seen that the maximum normal stresses are in the apex and base region and have a wavy distribution along the axial direction. We selected shear stresses FS and FN (according to Fig. 2) as the maximum stresses among all six components; they have a wavy distribution along the line AB.

Since the experimental curves of the Holzapfel experiments in Figs. 1B and 2B have hysteretic character, it is interesting to have an insight into the value of deformation energy within a cycle. Our model (the first one that takes hysteretic constitutive relations) gives a possibility to evaluate the deformation energy. Fig. 11C shows the change of deformation energy over the cycle: it increases during diastole and decreases during systole since the geometry of the wall comes back to the initial configuration. If there were no hysteresis, the deformation energy would come to zero. However, there is remaining energy, hysteretic energy (HE), shown in the figure.

Our model shows that the maximum energy (ME) is ME=28.02 *Ncm* and hysteretic energy is HE=2.57 *Ncm*; hence the HE is around 9% of the ME. The ratio HE/ME can be considered as a measure of the excessive energy needed from the muscle action to return the wall to the stress-free configuration. The strain energy at time $T$ is calculated as

$$W(T)=\sum_{n=1}^{N_T}\Delta W_n=\sum_{n=1}^{N_T}\int_V\frac{1}{2}\left(\sigma_i^t+\sigma_i^{t+\Delta t}\right)_n\left(\Delta e_i\right)_n,\quad sum\ on\ i:\ i=1,...,9 \tag{49}$$

where $N_T$ is a number of computational time steps used to reach time $T$, $V$ is the volume of the wall tissue, $\sigma_i^t$ and $\sigma_i^{t+\Delta t}$ are stress components at start and end of time step; $\Delta e_i$ include increments of normal strains in the fiber and sheet directions and amount of shear according to equation (24).

Finally, in order to have a complete picture of the mechanics of the LV, we computed the fluid flow field that follows from the echocardiogram recording. In this fluid model, we use the boundary conditions as follows. At the LV internal lateral surface, we calculate velocities from the displacements used for modeling the wall deformation, while for the top of the model velocities follow from the deformation due to the interaction with the fluid. At the mitral and aortic valve, we use prescribed pressures shown in Fig. 12A. During diastole, the aortic valve remains closed, hence velocity is equal to zero, while in the systole phase velocity at the mitral valve is equal to zero.

Fields of velocity and pressure are shown in Fig. 12B it the middle part of the systole. Pressure is close to uniform, while velocities decrease from the apex to the base. Fig. 12C displays the change of the mean pressure over the cycle and Fig. 12D displays the p-V diagram, which is close to the usually recorded.

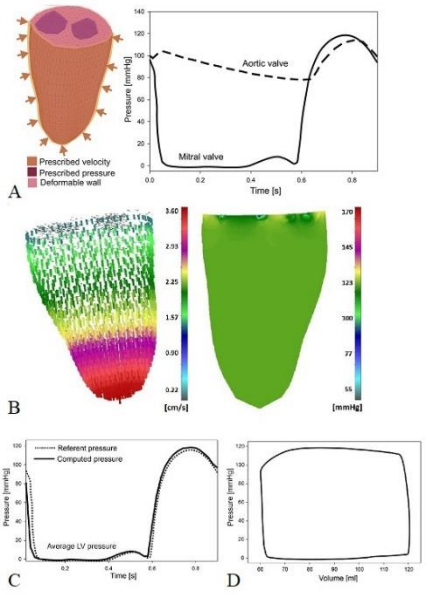


**Fig. 12.** (A) Fluid model boundary conditions; (B) Velocities within the LV and pressures at an axial (long) section (at time 0.76 s - middle of the systole); (C) Average pressure in the LV during a cardiac cycle, time is measured from the start of the diastole; (D) The pressure-volume (PV) diagram.

## 5. Summary and concluding remarks

We have introduced a finite element computational methodology to model the deformation of the left ventricle wall by directly using experimentally measured constitutive relationships. Several key tasks had to be solved in addition to the procedure of stress interpolation in the loading and reverse loading regimes. The first one was how to couple the stress-strain laws for the normal components. This was achieved by either imposing the incompressibility condition for the material – this was done by a penalty method or by employing a compressibility law according to experimental data. The second case is treated by introducing a novel concept of splitting deformation into deviatoric and volumetric parts. Then, the accuracy of the computational methodology was assessed on simple examples. The next task involved the development of a procedure to generate a 3D FE mesh of the LV wall from the echocardiograms. We use the geometry of the internal surface, which is generated from the echo-data; hence positions of the FE nodes at this surface have to be determined over the entire cycle. To achieve that, we have introduced a procedure consisting of two steps: a) the spatial positions of the FE nodes at the surface (the number of these nodes is constant over the cycle) is determined from the echocardiogram data, and b) the positions are corrected due to the LV torsion. Fluid flow within the LV is calculated using appropriate boundary conditions that follow from the model for the wall deformation and with prescribed pressures at the mitral and aortic valve.

The presented modeling approach of the mechanics of the LV can serve as the basis for practical applications since it relies on the true experimental constitutive relationships without any parameter fitting. Additionally, hysteretic characteristics of the tissue deformation are included for the first time, which may yield insight into the mechanical deformation energies during heart cycles. The presented computational model for mechanics can be directly coupled with our new methodology for electrophysiology and drug delivery (Kojic Transport Model; Kojic, 2018; Kojic et al., 2021). These multidisciplinary and multiscale models offer a basis for more reliable *in silico* clinical studies of heart problems, which may result in improved heart therapeutics.

**Acknowledgements** This work is supported by the grant NCI U54 CA210181, and by the SILICOFCM project that has received funding from the European Union's Horizon 2020 research and innovation programme under grant agreement No 777204. The research was also funded by the Serbian Ministry of Education, Science, and Technological Development, grants [451-03-9/2021-14/200378 (Institute for Information Technologies, University of Kragujevac)] and [451-03-9/2021-14/200107 (Faculty of Engineering, University of Kragujevac)]. The authors acknowledge support from the City of Kragujevac, Serbia.

## References

Bathe K. J. (1996). Finite Element Procedures, Englewood Cliffs, USA.

Bovendeerd P. H. M., Arts T., Huyghe J. M., Van Campen D. H. and Reneman R. S. (1992). Dependence of local left ventricular wall mechanics on myocardial fiber orientation: a model study, J. Biomechanics 2.5,1129-1140, doi.org/10.1016/0021-9290(92)90069-D.

Dokos S., LeGrice I. J., Smaill B. H., Kar J., Young A. A. (2000). A Triaxial-Measurement Shear-Test Device for Soft Biological Tissues, J. Biomech. Enrg, Trans. ASME 122, 471-478, doi.org/10.1115/1.1289624.

Dokos S., Smaill B. H., Young A. A., LeGrice I. J. (2002). Shear properties of passive ventricular myocardium, Am J Physiol Heart Circ Physiol 283, 2650–2659, doi.org/10.1152/ajpheart.00111.2002.

Fung Y. C., Fronek K. and Patitucci P. (1979). Pseudoelasticity of arteries and the choice of its mathematical expression, Am. J. Physiol. 237, 620-631, doi.org/10.1152/ajpheart.1979.237.5.h620.

Guccione J. M., McCulloch A. D., Waldman L. K. (1991). Passive Material Properties of Intact Ventricular Myocardium, J. Biomech. Engrg., Trans. ASME 113, 42-55, doi.org/10.1115/1.2894084.

Holzapfel G. A and Ogden R. W. (2009). Constitutive modelling of passive myocardium: a structurally based framework for material characterization, Phil. Trans. R. Soc. A 367, 3445–3475, doi.org/10.1098/rsta.2009.0091.

Humphrey J. D., Strumpf R.K., Yin F.C.P. (1990). Determination of a constitutive relation for passive myocardium I, A new functional form, J. Biomech. Enrg, Trans. ASME 112, 333-339, doi.org/10.1115/1.2891193.

Klepach D., Lee L. C., Wenk J. F., Ratcliffe M. B., Zohdi T. I., Navia J. L., Kassab G. S., Kuhl E., Guccione J. M. (2012). Growth and remodeling of the left ventricle: A case study of myocardial infarction and surgical ventricular restoration, Mech. Res. Communications 42, 134-141, doi.org/10.1016/j.mechrescom.2012.03.005.

Klotz S., Hay I., Dickstein M. L., Yi G-H, Wang J., Maurer M. S., Kass D. A., Burkhoff D. (2006). Single-beat estimation of end-diastolic pressure-volume relationship: a novel method with potential for noninvasive application, Am. J. Physiol. Heart Circ. Physiol. 291, 403–412, doi.org/10.1152/ajpheart.01240.2005.

Kojic M. (2018). Smeared concept as a general methodology in finite element modeling of physical fields and mechanical problems in composite media, J. Serb. Soc. Comp. Mech. 12, 1-16, doi.org/10.24874/jsscm.2018.12.02.01.

Kojic M. and Bathe K. J. (2005). Inelastic Analysis of Solids and Structures, Springer, Heidelberg-Berlin-New York.

Kojic M., Filipovic N., Stojanovic B., Kojic N. (2008). Computer Modeling in Bioengineering, Chichester: J. Wiley and Sons.

Kojic M., Milosevic M., Filipovic N. (2018). PAK-BIO, Finite element program for bioengineering problems, Bioengineering Research and Development Center BioIRC and University of Kragujevac, Serbia.

Kojic M., Milosevic M., Ziemys A. (2021). Computational Models in Biomedical Engineering - Finite Element Models Based on Smeared Physical Fields: Theory, Solutions, and Software, Elsevier, (to be published).

Krishnamurthy A. and Kerckhoffs R. C. P. (2013). Patient-specific models of cardiac biomechanics, J. Comput. Physics 244, 4–21, doi.org/10.1016/j.jcp.2012.09.015.

Lang R.M., Badano L.P., Mor-Avi V., Afilalo J., Armstrong A., Ernande L., et al. (2015). Recommendations for Cardiac Chamber Quantification by Echocardiography in Adults: An Update from the American Society of Echocardiography and the European Association of Cardiovascular Imaging. J Am Soc Echocardiogr 28, 1-39, doi.org/10.1016/j.echo.2014.10.003.

Leonard B. L., Smaill B. H. and LeGrice I. J. (2012). Structural remodeling and mechanical function in Heart Failure, Microsc. Microanal. 18, 50–67, doi.org/10.1017/S1431927611012438.

Lin D. H. S., Yin F.C. P. (1998). A multiaxial constitutive law for mammalian left ventricular myocardium in steady-state barium contracture or tetanus, J Biomech Eng. 120, 504-517, doi.org/10.1115/1.2798021.

McEvoy E., Holzapfel G.A., McGarry P. (2018). Compressibility and anisotropy of the ventricular myocardium: Experimental analysis and microstructural modeling, Journal of Biomechanical Engineering 140, doi.org/10.1115/1.4039947.

Ponnaluri A.V.S., Perotti L.E., Ennis D.B., Klug W.S. (2017). A viscoactive constitutive modeling framework with variational updates for the myocardium, Comput. Methods Appl. Mech. Engrg. 314, 85–101, doi.org/10.1016/j.cma.2016.09.022.

Salem Omar A.M., Vallabhajosyula S., Sengupta P. P. (2015). Left Ventricular Twist and Torsion, Cardiovasc Imaging 8, 74-82, doi.org/10.1161/CIRCIMAGING.115.003029.

Sommer G., Schriefl A. J., Andrä M., Sacherer M., Viertler C., Wolinski H., Holzapfel G. A. (2015). Biomechanical properties and microstructure of human ventricular myocardium, Acta Biomaterialia 24, 172–192. doi.org/10.1016/j.actbio.2015.06.031.

Stevens C., Remme E., LeGrice I., Hunter P. (2003). Ventricular mechanics in diastole: material parameter sensitivity, J. Biomechanics 36, 737–748, doi.org/10.1016/s0021-9290(02)00452-9.

Xi J., Lamata P., Niederer S., Land S., Shi W., Zhuang X., et al. (2013). The estimation of patient-specific cardiac diastolic functions from clinical measurements, Medical Image Analysis 17, 133-146, doi.org/10.1016/j.media.2012.08.001.

Yeoh O. H. (1993). Some forms of the strain energy function for rubber, Rubber Chem. Technol. 66, 754–771, doi.org/10.5254/1.3538343.

Yin F. C. P., Strumpf R. K., Chew P. H. and Zeger S. L. (1987). Quantification of the mechanical properties of noncontracting canine myocardium under simultaneous biaxial loading, J. Biomechanics 20, 577-589, doi.org/10.1016/0021-9290(87)90279-x.